Multimodal analysis of force spectroscopy based on a transfer function study of micro-cantilevers

Rafael Vázquez[1,3]**, F Javier Rubio-Sierra**[2] **and Robert W Stark**[2]

[1] MAE Department, University of California at San Diego, La Jolla, CA 92093-0411, USA
[2] CeNS and Section Crystallography, Department of Earth and Environment,
Ludwig-Maximilians-Universität München, Theresienstraße 41, D-80333 Munich, Germany

E-mail: rvazquez1@us.es and stark@lmu.de

Abstract

Quantitative force spectroscopy experiments require a comprehensive
knowledge of the frequency response characteristics of the micro-cantilever.
To establish a generic theoretical model an analytical mathematical
description of the cantilever dynamics in force spectroscopy was developed
using a transfer function approach. This study allows for quantitative
evaluation of force spectroscopy experiments and analysis of stability and
controllability of an atomic force microscope (AFM). The model accounts
for the dynamic characteristics of the extended cantilever beam and for
elastic sample properties. The system dynamics were investigated using an
exact system-theoretic approach. The step and frequency responses are given
for force spectroscopy experiments in different experimental configurations.
The transfer function approach used in this study allows us to investigate very
significant dynamic aspects that simple first mode approximations cannot
capture. Only extended beam models account for both poles and zeros of the
transfer function and can thus reproduce important features that are related to
the zero dynamics. These features include pole-zero cancellations or
non-minimum phase response. The possibility of non-minimum phase
response in AFM is highly important for the design of inverse filters. The
presence of zeros in the right half of the Laplace plane immediately implies
that the inverse system is unstable.

1. Introduction

For a quantitative analysis of force spectroscopy experiments
in atomic force microscopy (AFM) a full mathematical
description of the dynamic response is required. Such a
mathematical model has to account for the characteristics
of the extended cantilever beam together with the sample
properties. Two different experimental approaches are of
special interest: force pulling and small amplitude force
modulation. Pulling experiments include molecular force
spectroscopy [1] or the molecular force clamp [2, 3]. The
small signal response to a mechanical stimulus can be obtained
from noise analysis [4, 5] or by active q-spectroscopy [6]. In
the latter method viscoelastic properties are extracted from the
system response to a small external forcing at resonance. A
special feedback system (q-control) undamps the system and
helps to track the resonant frequency. The dynamic response
of the AFM cantilever in a pulling/pushing experiment can
be understood by analysing the step response of the system;
the response in a modulation experiment can be visualized in
a Bode plot [7] which depicts amplitude and phase response
as a function of the frequency. The dynamics observed in
both experimental configurations are intimately connected by
the transfer characteristics of the system. Additionally, a
theoretical description that includes a characterization of poles-
zeros dynamics enables us to analyse the regimes of system

[3] Present address: Departamento de Ingeniería Aeroespacial, Escuela Supe-
rior de Ingenieros, Universidad de Sevilla, Avenida de los Descubrimientos
s.n., E-41092 Seville, Spain.

stability along with a determination of the non-minimum phase character of the system. The non-minimum phase character of the system is of critical importance for the reconstruction of forces acting on the cantilever tip [8–10] and the design of inverse filters necessary for model based estimation of tip–sample interaction [11] and control of forces in nanolithography [12].

Thus, modelling of the dynamics corresponding to an AFM cantilever interacting with the sample is paramount for dynamic AFM based methods. There are several approaches to model the AFM cantilever. The simplest rely on modelling the cantilever as a single-degree-of-freedom harmonic oscillator, the so-called first mode approximation [13]. Although the first mode approximation is very useful for special applications such as simulation of phase imaging AFM [14] or state estimation in amplitude modulation AFM [11], it does not take into account that the cantilever is a distributed parameter system with an infinite number of resonant frequencies. The higher modes are of great importance for excitation of the cantilever at frequencies above the first resonance [15]. The use of a lumped-parameter model avoids the limitation of the first mode approximation including a finite number of resonant modes [16]. The Euler–Bernoulli beam equation provides a complete infinite-dimensional description of the problem. The infinite product expansion goes beyond lumped parameter models as it allows us to obtain an exact expression for all the poles and zeros of the system. This is an improvement in comparison to the lumped-parameter model where the numerical values of the system zeros only slowly converge to the exact value with an increased number of poles included in the analysis. However, if damping or tip–sample interaction are included, the solution of the infinite dimensional problem is not trivial [17–19].

Transfer function analysis is an approach to analyse distributed systems which easily delivers a complete description of system dynamics. Additionally, it also represents a useful tool to study the effects of system configuration (placement of inputs and outputs) in modelling and control design of flexible systems by pole and zero analysis [20]. The transfer functions of distributed systems consist in transcendental functions; therefore, in order to obtain an analytical expression of system poles and zeros, infinite product expansions must be found [21]. Recently, we have applied the transfer function approach to obtain a dynamic description of the free AFM cantilever without tip–sample interaction [22].

In the following analysis we consider a typical rectangular AFM cantilever subject to a linearized variable interaction corresponding either to a tethered molecule or a surface. This analysis includes a free or a pinned end as limit cases. The influence of different system configurations on the system dynamics is highlighted by modelling the AFM cantilever as a multiple-input–multiple-output (MIMO) system. The inputs are point load and distributed force, while the outputs are position and slope along the cantilever. From the resulting transfer function matrix, the dynamics of the system are discussed using Bode plot representation, poles and zero locus plot, and transient response to a step force input. The influence of the force gradient at the tip–sample contact on the frequency response are discussed in detail. This analysis includes non-minimum phase behaviour, stability and controllability of the
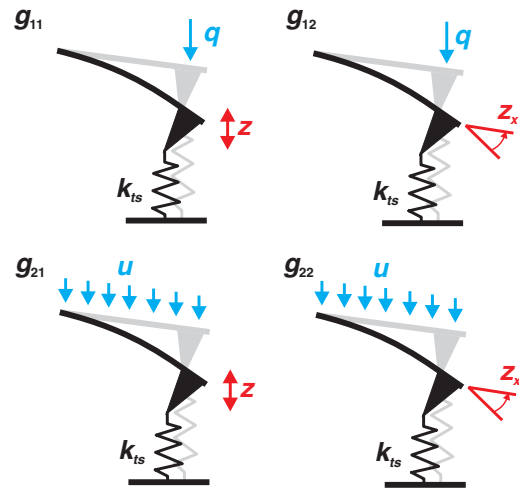
Figure 1. Different inputs (blue) and outputs (red) of the mechanical system as considered in the MIMO system.

system. The consequences on AFM operation and force spectroscopy measurements are discussed in detail.

2. Cantilever system description

We assume an AFM cantilever of length L, width w and thickness d with a constant cross section. The transversal displacement of the cantilever relative to its support is described by the variable $z(t, x)$ defined positive for a displacement toward the sample, where t is time, $x \in [0, L]$ the position. $x = 0$ is the fixed end of the cantilever and $x = L$ the free end. The force gradient corresponding to surface bonding of the AFM tip is considered in the boundary conditions. As illustrated in figure 1 the inputs and outputs of the system under consideration are the following:

- Input 1, $q(t)$, is an external force acting at the tip end. Such a force can be generated, for example, by conformational fluctuations of a molecule under test or a magnetic particle attached at the tip end which is then actuated by generating a magnetic field [23].
- Input 2, $u(t)$, is a distributed force per unit length acting along the cantilever, which corresponds to an inertial force generated by a mechanical excitation produced by a piezoelectric transducer [24], an electrostatic force or thermal excitation [25].
- Output 1, $z(t, L)$, is the vertical deflection at the free end, measurable by interferometric methods [26]. Although this measurement is not usual in commercial AFM systems, it plays an important role because it provides a direct measurement of the tip deflection and the tip sample forces.
- Output 2, $z_x(t, L)$, is the deflection slope measured at the free end of the cantilever, which is measured using the bouncing beam detection method [27]. This represents an idealized output in standard AFM systems based on the light lever detection scheme.

Considering the cantilever as a MIMO system, we can write its (matrix) transfer function description as

$$\begin{bmatrix} Z(s, L) \\ Z_x(s, L) \end{bmatrix} = G(s) \begin{bmatrix} U(s) \\ Q(s) \end{bmatrix}, \tag{1}$$

where $Z(s, L)$, $Z_x(s, L)$, $U(s)$ and $Q(s)$ stand, respectively, for the Laplace transformed vertical deflection $z(t, L)$, slope $z_x(t, L)$, distributed force $u(t)$ and force at the tip $q(t)$, s is the Laplace variable (with units of frequency) and $G(s)$ is the matrix transfer function of the system,

$$G(s) = \begin{pmatrix} g_{11} & g_{12} \\ g_{21} & g_{22} \end{pmatrix}. \tag{2}$$

Here, $g_{ij}(s)$ represents the transfer function of input i to output j.

3. Tip–surface interaction

In this work we consider a linear approximation of the tip–sample interaction modelled by an effective force constant. From an experimental point of view this approximation is justified in the case of a very small dithering of the tip position or for the description of the thermo-mechanically oscillating cantilever. For the case where the tip of the cantilever is attached to a surface through a tethered molecule, the effective force constant is given by the force constant of the molecule [1] and the correspondent effective tip–sample stiffness by the corresponding force gradient. If we consider the case where the tip is directly interacting with a surface, then an elastic contact model can be used to calculate the effective force constant.

For a rigid solid surface, the mechanical tip–sample interaction can be modelled by a Derjaguin–Mueller–Toporov (DMT) model neglecting damping in the tip–sample contact. The interaction force is a nonlinear function that depends mainly on the proximity of the tip to the sample [28]. Calling $z_s(z)$ the distance from the sample to the free end of the undeflected cantilever, the true tip–surface distance neglecting sample deformation is given by $z_s(t) - z(t, L)$. Denominating $f(t)$ as the tip–surface interaction force and a_0 the interatomic distance, one can characterize two regimes of behaviour. If $z_s(t) - z(t, L) \geqslant a_0$, the force is attractive and can be described by a van der Waals model,

$$f(t) = -\frac{HR}{6(z_s(t) - z(t, L))^2}. \tag{3}$$

If $z_s(t) - z(t, L) < a_0$, the interaction is repulsive and can be computed using a DMT model,

$$f(t) = -\frac{HR}{6a_0^2} + \frac{4}{3}E^*\sqrt{R}(z_s(t) - z(t, L) + a_0)^{3/2}. \tag{4}$$

In (3) and (4), H represents the Hamaker constant, R the tip radius and E^* the effective contact stiffness, which can be derived from the elastic moduli of tip and sample (respectively E_t and E_s) and their Poisson ratios (resp. ν_t and ν_s), using the following expression: $E^* = [(1 - \nu_t^2)/E_t + (1 - \nu_s^2)/E_s]^{-1}$. For the transfer function analysis, we will consider the case in which the system stays in the close neighbourhood of an equilibrium set point z_0, which can be adjusted by moving the

sample relative to the cantilever mount [29]. Linearizing the force around the set point, we obtain

$$f(t) = -k_{ts}z(t, L), \tag{5}$$

where

$$k_{ts} = -\left.\frac{\partial f(t)}{\partial z(t, L)}\right|_{z_0}, \tag{6}$$

represents the effective force constant. Inserting (3) and (4) into (5), we find

$$k_{ts}$$
$$= \begin{cases} -HR/3(z_s(t) - z_0)^3, & \text{if } z_s(t) - z(t, L) \geqslant a_0, \\ 2E^*\sqrt{R(z_s(t) - z_0 + a_0)}, & \text{if } z_s(t) - z(t, L) < a_0. \end{cases} \tag{7}$$

Note that the sign of k_{ts} depends on the regime of the force. For the attractive regime one, the constant is negative, while for the repulsive regime the constant is positive. We consider

$$k_{ts} = \frac{3EI}{L^3}\hat{k}_{ts}, \tag{8}$$

where E is the Young modulus and $I = wd^3/12$ is the area moment of inertia. The quantity $3EI/L^3$ corresponds to the cantilever spring constant. Then $\hat{k}_{ts}$ is the parameter that determines the magnitude and regime of the force. In this work we shall consider all possible values of $\hat{k}_{ts}$ including zero (free end) and infinity (pinned end). In order to focus the discussion on the cantilever dynamics we will only consider elastic interaction and neglect damping in the tip and sample contact.

4. Dynamic model of the cantilever interacting with a surface

The dynamics of the surface-coupled AFM cantilever can be derived from the classical Euler–Bernoulli beam equation, in which we neglect rotary inertia, axial effects, shear deformation and tip mass, but include damping effects,

$$EI\frac{\partial^4 z}{\partial x^4} + c\frac{\partial z}{\partial t} + m\frac{\partial^2 z}{\partial t^2} = -u(t), \tag{9}$$

where m corresponds to the mass per unit length. The damping factor c is due to both the internal cantilever friction and the surrounding media. If there is no base motion of the cantilever, then both effects are included in c. However, if the cantilever base is moved in order to induce an inertial force on the cantilever, then a first order approach must be used to model the damping factor in (9):

$$EI\frac{\partial^4 z}{\partial x^4} + c_e\left(\frac{\partial z}{\partial t} + \frac{\partial z_b}{\partial t}\right) + m\frac{\partial^2 z}{\partial t^2} = -u(t), \tag{10}$$

where c_e corresponds to an effective damping constant and $z_b(t)$ to the position of the cantilever base.

The boundary conditions at the fixed end are zero deflection and zero slope:

$$z(t, 0) = 0, \qquad \left.\frac{\partial z}{\partial x}\right|_{x=0} = 0. \tag{11}$$

3

At the free end no torque is assumed,

$$\frac{\partial^2 z}{\partial x^2}\bigg|_{x=L} = 0, \qquad EI\frac{\partial^3 z}{\partial x^3}\bigg|_{x=L} + f(t) = -q(t). \quad (12)$$

We have included both the interaction force $f(t)$ and the input $q(t)$. Introducing the linearized force (5)–(8) in (12) yields

$$EI\left(\frac{\partial^3 z}{\partial x^3}\bigg|_{x=L} - \frac{3\hat{k}_{ts}}{L^3}z(t,L)\right) = -q(t). \quad (13)$$

Following [22], we take the Laplace transform, disregarding initial conditions and seek a solution of the form

$$\begin{aligned}
Z(s,x) &= \cosh(\lambda(s)x)\left[A\cos(\lambda(s)x) + B\sin(\lambda(s)x)\right] \\
&\quad + \sinh(\lambda(s)x)\left[C\cos(\lambda(s)x) + D\sin(\lambda(s)x)\right] \\
&\quad + \frac{U(s)}{4EI\lambda(s)^4}, \quad (14)
\end{aligned}$$

where s is the Laplace variable (frequency), and

$$\lambda(s) = \sqrt[4]{\frac{cs + ms^2}{4EI}}. \quad (15)$$

The constants A, B, C, and D can be found by substitution in the boundary conditions (11) and (12). Once the solution $Z(s,x)$ is found, the slope is obtained as $Z_x(s,x) = \partial Z/\partial x$. We skip the long analytic expression for the solutions for $Z(s,x)$ and $Z_x(s,x)$, which can be found by using any commercial symbolic calculation package.

For numerical calculations and plots, we have employed the following numerical data unless otherwise explicitly indicated: $E = 169$ GPa, $m = 3.72 \times 10^{-7}$ kg m^{-1}, $L = 232$ μm, $w = 40$ μm, $d = 4$ μm and $c = 0.01$ kg ms^{-1}. For the discussion of the transfer characteristics as a function of the effective tip–sample stiffness the parameter range is $-1 \leqslant \hat{k}_{ts} < \infty$. For further numerical simulations of the nonlinear system one can use the Hamaker constant $H = 6.4 \times 10^{-20}$ J and the distance $a_0 = 0.166$ nm.

In the following, we do not write the dependence on the Laplace variable s explicitly.

5. Transfer functions of the system

The matrix transfer function of the system, G, as defined in (1) and (2) can be found by evaluating the solutions $Z(x)$ and $Z_x(x)$ at $x = L$. Its expression is

$$G = \frac{1}{D}\begin{pmatrix} n_{11} & n_{12} \\ n_{21} & n_{22} \end{pmatrix}, \quad (16)$$
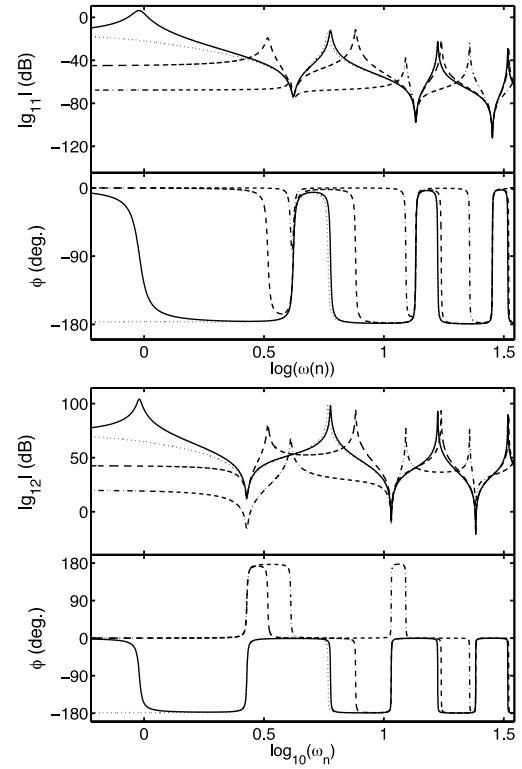
where the common denominator D is

$$\begin{aligned}
D = EI\{&2[2 + \cos(2\lambda L) + \cosh(2\lambda L)] \\
&+ \frac{3\hat{k}_{ts}}{L^3\lambda^3}[\sinh(2\lambda L) - \sin(2\lambda L)]\}, \quad (17)
\end{aligned}$$

and the numerator values are:

$$n_{11} = \frac{1}{\lambda^3}[\sinh(2\lambda L) - \sin(2\lambda L)], \quad (18)$$

$$n_{12} = \frac{1}{\lambda^2}[\cosh(2\lambda L) - \cos(2\lambda L)], \quad (19)$$

$$n_{21} = \frac{-1}{2\lambda^4}[\cos(\lambda L) - \cosh(\lambda L)]^2, \quad (20)$$

Figure 2. Bode plots of g_{11} (top) and g_{12} (bottom) for $\hat{k}_{ts} = -1, 0, 10, 100$ (respectively dotted, solid, dashed and dashed–dotted lines).

$$\begin{aligned}
n_{22} = &\frac{-2}{\lambda^3}[\cosh(\lambda L)\sin(\lambda L) - \cos(\lambda L)\sinh(\lambda L)] \\
&+ \frac{3\hat{k}_{ts}}{2L^3\lambda^6}[\sin(\lambda L) - \sinh(\lambda L)]^2. \quad (21)
\end{aligned}$$

Note that the only expressions depending on $\hat{k}_{ts}$ are D and n_{22}.

5.1. Frequency response

We study each subsystem g_{ij} separately. From the expressions of the different transfer functions it is straightforward to obtain the frequency response of the system using the Bode plot representation [7]. The response amplitude at a given angular frequency ω is given by the module of the complex valued transfer function $|g_{ij}(j\omega)|$, while the phase shift ϕ corresponds to the angle $\angle g_{ij}(j\omega)$. Bode plots are shown in figures 2 and 3 for values $\hat{k}_{ts} = -1, 0, 10, 100$. We do not show the frequency response for $\hat{k}_{ts} < -1$, since that range of values is shown in section 6 to lead to an instable system.

The great influence of the I/O configuration and the magnitude of the contact stiffness on the frequency response of the system is manifested in the Bode plots. The most interesting qualitative feature of the plots is the attenuation and displacement of resonant modes to the right, as $\hat{k}_{ts}$ increases. It is also worth noting that, for all the subsystems considered except the one corresponding to g_{22}, the phase shift is finite (even though there is an infinite number of zeros, their location is such that their respective phase contribution compensates). For any finite value of $\hat{k}_{ts}$, the phase shift for g_{22} is always
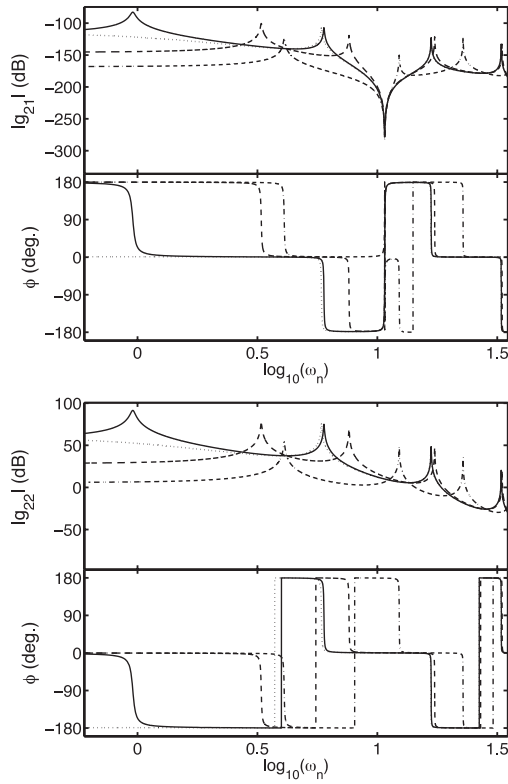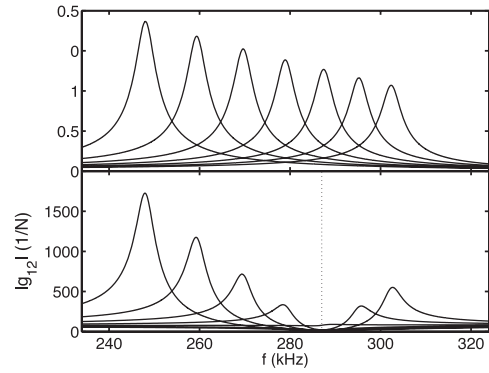
Figure 3. Bode plots of g_{21} (top) and g_{22} (bottom) for $\hat{k}_{ts} = -1, 0, 10, 100$ (respectively dotted, solid, dashed and dashed–dotted lines). The sharp edges in the phase shift of g_{22} are due to the continuity from $-180°$ to $180°$.

Figure 4. Shift of the resonance curve for both outputs of the system due to different values of $\hat{k}_{ts}$ for the point load input. The values of $\hat{k}_{ts}$ for the different resonance curves from left to right are 6.1, 7.0, 7.8, 8.7, 9.5, 10.4 and 11.2. For the slope output, the resonance vanishes due to a system antiresonance located at $f = 287$ kHz (marked with a line in the graph).

Figure 5. Shift of the resonance curve for both outputs of the system due to different values of $\hat{k}_{ts}$ for the distributed force input. The values of $\hat{k}_{ts}$ for the different resonance curves from left to right span from 0 (free oscillations) to 2.4 with increments of 0.4.
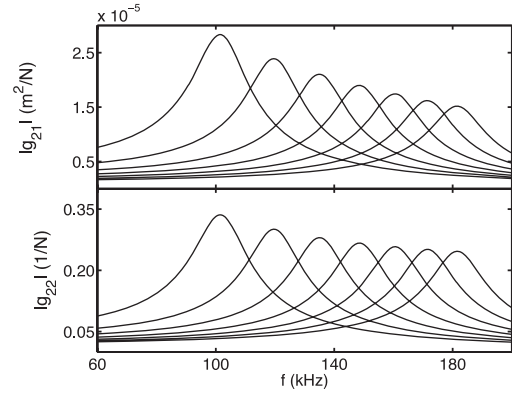
increasing and tends to infinity when the frequency grows. In section 7, it will be shown that this increase in phase is due to an infinite number of right-half plane zeros (non-minimum phase zeros).

In some cases there are modes of resonance that get strongly attenuated, almost disappearing or exchanging its position with one antiresonance. This is the effect of an (stable) pole-zero cancellation that happens for a close value of $\hat{k}_{ts}$. The cancellation may change dramatically the behaviour of the system in the frequency range of the disappearing resonance mode. Figure 4 shows the first resonance peak for different values of $\hat{k}_{ts}$ in the point load configuration. For both outputs, the resonance peak is shifted for increasing contact stiffness, in a similar way as predicted by the simple harmonic oscillator model. However, the response for the slope output is dramatically changed. The cancellation of the system resonance is due to the antiresonance at the frequency $f = 287$ kHz. Note that the position of the antiresonances depends only on the used cantilever and not on the interaction with the surface for all system configurations except for the subsystem with distributed force and slope output (g_{22}).

The force modulation spectroscopy has been developed to perform direct measurement of single-molecule stiffness and viscoelasticity with the AFM [5]. In this measurement a stochastic distributed force due to the thermal excitation acts on the cantilever while the tethered molecule generates the interaction force at the cantilever end. Figure 5 shows the shift of the first resonant peak for both outputs of the distributed

force input with $\hat{k}_{ts}$ ranging from 0 to 2.4. The damping was set to $c = 0.04$ to account for a stronger damping. The position output suffers a higher magnitude decrease than the slope output due to the reduction of the cantilever amplitudes of vibration with higher stiffness.

5.2. Limit cases

There are two limit cases corresponding to a freely oscillating cantilever and to a cantilever pinned at its end:
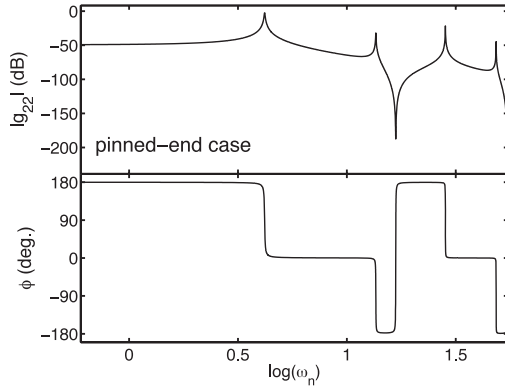
$$G^0 = \lim_{\hat{k}_{ts} \to 0} G, \tag{22}$$

$$G^\infty = \lim_{\hat{k}_{ts} \to \infty} G. \tag{23}$$

The transfer functions for these limit cases are

$$G^0 = \frac{1}{D^0} \begin{pmatrix} n_{11} & n_{12} \\ n_{21} & n_{22}^0 \end{pmatrix}, \tag{24}$$

Figure 6. Bode plot of g_{22} (top) for the special case where the end of the cantilever is pinned to the surface ($\hat{k}_{ts} = \infty$).

and

$$G^\infty = \frac{1}{D^\infty} \begin{pmatrix} 0 & 0 \\ 0 & n_{22}^\infty \end{pmatrix}, \qquad (25)$$

where

$$D^0 = 2EI\left(2 + \cos\left(2\lambda L\right) + \cosh\left(2\lambda L\right)\right), \qquad (26)$$

$$n_{22}^0 = \frac{-2}{\lambda^3}\left(\cosh\left(\lambda L\right)\sin\left(\lambda L\right) - \sinh\left(\lambda L\right)\cos\left(\lambda L\right)\right), \quad (27)$$

$$D^\infty = \frac{2EI}{L^3\lambda^3}\left(\sinh\left(2\lambda L\right) - \sin\left(2\lambda L\right)\right), \qquad (28)$$

$$n_{22}^\infty = \frac{-1}{L^3\lambda^6}\left(\sin\left(\lambda L\right) - \sinh\left(\lambda L\right)\right)^2. \qquad (29)$$

A detailed analysis of the freely vibrating cantilever (24) has already been presented elsewhere, see [22] and references therein. In the pinned cantilever case, all the components of the transfer function matrix (25) are zero except the component corresponding to the distributed force input with slope output case. The Bode plot corresponding to this nonzero component is shown in figure 6. The most remarkable characteristic of the Bode plot figure is the appearance of antiresonances. The phase at the antiresonance is incremented by 360° and the phase shift remains limited, as the system is no more non-minimum in phase.

6. System poles

The poles of the system correspond to the complex roots of the denominator D in (17). The denominator is common to all the studied subsystems, due to the fact that the system poles are not affected by the selection of inputs and outputs. As our model is infinite-dimensional, to obtain an exact expression of system poles the denominator has to be written in form of an infinite product expansion [21]. One must distinguish three cases depending on $\hat{k}_{ts}$.

(i) If $\hat{k}_{ts} > -1$, then

$$D = C \prod_{n=1}^\infty \left[1 + \frac{4L^4\lambda^4}{d_n^4}\right]. \qquad (30)$$

(ii) If $\hat{k}_{ts} = -1$, then a root at zero must be added to (30),

$$D = \frac{88}{35}L^4\lambda^4 \prod_{n=1}^\infty \left[1 + \frac{4L^4\lambda^4}{d_n^4}\right]. \qquad (31)$$

(iii) If $\hat{k}_{ts} < -1$, the expression for the denominator is

$$D = C\left[1 - \frac{16L^4\lambda^4}{d_0^4}\right] \prod_{n=1}^\infty \left[1 + \frac{4L^4\lambda^4}{d_n^4}\right]. \qquad (32)$$

In (30)–(32), $C = 8EI(1 + \hat{k}_{ts})$, d_n is the infinite sequence of increasingly ordered real positive solutions of the transcendental equation

$$\frac{3\hat{k}_{ts}}{d_n^3}\left[\sinh d_n \cos d_n - \cosh d_n \sin d_n\right]$$
$$= 1 + \cos d_n \cosh d_n, \qquad (33)$$

and d_0 is the only real, positive solution of the following equation:

$$2 + \cos d_0 + \cosh d_0 = -\frac{12\hat{k}_{ts}}{d_0^3}(\sinh d_0 - \sin d_0). \qquad (34)$$

Note that C, d_n and d_0 are all parametrized by $\hat{k}_{ts}$.

Substituting now the value of $\lambda(s)$ from (15) in expressions (30)–(32), it is possible to find the location of the poles for all three cases. For all values of $\hat{k}_{ts}$, there are poles verifying

$$\frac{cs_{\text{poles}} + ms_{\text{poles}}^2}{EI} = -\frac{d_n^4}{L^4}, \qquad (35)$$

and solving for s_{poles},

$$s_{\text{poles}} = -\frac{c}{2m} \pm \sqrt{\frac{c^2}{4m^2} - \frac{EI d_n^4}{mL^4}}, \qquad (36)$$

which, for c smaller than d_n, yields a pair of complex conjugated roots.

For case ii, in addition to the poles given by (36), there is one additional pole at the origin and another pole located at $-c/m$.

In case iii, in addition to the poles in (36), there are two real poles, one with negative real part and another with positive real part (instable pole),

$$s_{\text{poles}} = -\frac{c}{2m} \pm \sqrt{\frac{c^2}{4m^2} + \frac{EI d_0^4}{4mL^4}}. \qquad (37)$$

It is also interesting to obtain the poles for the limit cases. If $\hat{k}_{ts} = 0$, one gets the well known expression of the freely oscillating cantilever poles

$$D^0 = 8EI \prod_{n=1}^\infty \left[1 + \frac{4L^4\lambda^4}{b_n^4}\right], \qquad (38)$$

where now the b_n are the positive solutions of the equation

$$1 + \cos b_n \cosh b_n = 0, \qquad (39)$$

and the exact value of the poles is

$$s_{\text{poles}}^0 = -\frac{c}{2m} \pm \sqrt{\frac{c^2}{4m^2} - \frac{EI b_n^4}{mL^4}}, \qquad (40)$$

Table 1. Resonant frequencies of the first five modes of resonance for different values of the effective contact stiffness $\hat{k}_{ts}$.

$\hat{k}_{ts}$	Mode 1 f_1^{res} (kHz)	Mode 2 f_2^{res} (kHz)	Mode 3 f_3^{res} (kHz)	Mode 4 f_4^{res} (kHz)	Mode 5 f_5^{res} (kHz)
−0.5	72.8	636.8	1792.7	3515.0	5811.3
0.0	102.2	640.7	1794.1	3515.7	5811.7
1.0	142.5	648.8	1796.9	3517.1	5812.6
10.0	291.8	727.3	1823.5	3530.4	5820.5
100.0	426.5	1192.6	2144.4	3684.2	5906.7
∞	448.3	1452.9	3031.4	5183.9	7910.4

which yields pairs of (stable) complex conjugate poles. For $\hat{k}_{ts}$ tending to infinity, the denominator (28) can be expanded into

$$D^{\infty} = \frac{16EI}{3} \prod_{n=1}^{\infty} \left[1 + \frac{4L^4\lambda^4}{c_n} \right], \tag{41}$$

where c_n are the positive real solutions of

$$\tan c_n = \tanh c_n, \tag{42}$$

and the exact value of the poles is given by

$$s_{poles}^{\infty} = -\frac{c}{2m} \pm \sqrt{\frac{c^2}{4m^2} - \frac{EIc_n^4}{mL^4}}, \tag{43}$$

which yields pairs of complex conjugate poles in the left half plane (LHP) of the Laplace plane.

If the damping of each pole, i.e. its negative real part, is very small compared to the modulus of the pole, the resonant frequency f_n^{res} corresponding to each pair of conjugated poles can be approximated using the imaginary part of the poles,

$$f_n^{res} = \frac{Im(s_n)}{2\pi}. \tag{44}$$

This approximation is not valid in case i for the first pair of poles, calculated with d_1 from (33), if $\hat{k}_{ts}$ is close to −1. In that situation d_1 approaches zero and will be of the order of c. Table 1 shows the resonant frequency values for the first five resonant modes of vibration calculated using different contact stiffness.

For the numerical values given at the end of section 4, we represent the poles in figure 7, a root locus type of plot where we show how the position of the poles is altered by changing $\hat{k}_{ts}$. The poles for the limit cases alternate on a line parallel to the imaginary axis, located on the LHP. When $\hat{k}_{ts}$ increases from zero to infinity, the poles of the case $\hat{k}_{ts} = 0$ (circles in the diagram) increase their imaginary part, reaching in the limit the values of the case $\hat{k}_{ts} \to \infty$ (crosses in the diagram).

Analogously, for decreasing $\hat{k}_{ts}$ from zero to −∞, the imaginary part of the poles decreases as well. Poles of the case $\hat{k}_{ts} = 0$ move toward poles of the pinned end limit case, always staying in the LHP. The only exception is the first pair of poles of the case $\hat{k}_{ts} = 0$, whose imaginary part decrease till they become real (for $\hat{k}_{ts}$ approaching −1). At $\hat{k}_{ts} = -1$ one of them is located in the origin. Decreasing $\hat{k}_{ts}$ beyond −1 moves the pole further into the right half plane (RHP), making the system unstable. This instable behaviour for the range $\hat{k}_{ts} \in (-\infty, -1)$ (strongly attractive regime of the surface coupling force) corresponds to the physical
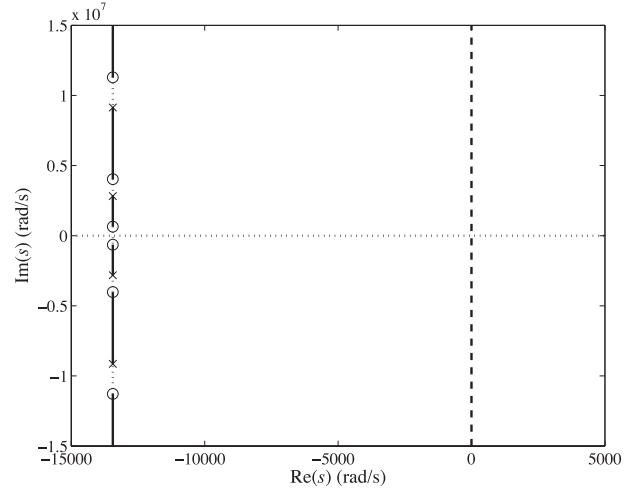
Figure 7. Location of poles with $\hat{k}_{ts}$. Circles mark poles at $\hat{k}_{ts} = 0$, crosses at $\hat{k}_{ts} \to \infty$. Solid lines and dotted lines describe, respectively, the movement of poles for positive and negative $\hat{k}_{ts}$. The dashed line is the imaginary axis.

phenomenon known as 'snap-in' [30]. When approaching the surface closely the cantilever can, suddenly, bend toward the surface due to the attractive van der Waals forces. This instability is stopped in the real nonlinear system by a change of regime to the repulsive zone of the coupling force.

7. System zeros

The zeros of the system correspond to the roots of the numerators (18)–(21). As the numerators n_{11}, n_{12} and n_{21} do not depend on the contact stiffness, the value of $\hat{k}_{ts}$ does not change the location of zeros for these subsystems and correspond to the free vibrating limit case. We refer to [22] for a detailed study. The only subsystem in which zeros are affected by changes in the contact stiffness corresponds to the numerator n_{22}. Here, two cases must be considered:

(i) If $\hat{k}_{ts} \neq 8$, n_{22} can be expanded as

$$n_{22} = -\frac{L^3}{6}(8 - \hat{k}_{ts}) \prod_{n=1}^{\infty} \left[1 - \frac{L^4\lambda^4}{z_n^4} \right]. \tag{45}$$

(ii) If $\hat{k}_{ts} = 8$, then a root at zero must be added, so

$$n_{22} = \frac{-L^7\lambda^4}{105} \prod_{n=1}^{\infty} \left[1 - \frac{L^4\lambda^4}{z_n^4} \right]. \tag{46}$$

In expressions (45) and (46), z_n is the infinite sequence of nonzero complex solutions, located in the first quadrant of the imaginary plane (positive real and imaginary part) and ordered by increasing absolute value, of the complex equation:

$$4z_n^3 [\cosh(z_n)\sin(z_n) - \sinh(z_n)\cos(z_n)]$$
$$= 3\hat{k}_{ts} [\sin(z_n) - \sinh(z_n)]^2. \tag{47}$$

Substituting (15) in (45) and (46), we find that the zeros are located at

$$s_{zeros} = -\frac{c}{2m} \pm \sqrt{\frac{c^2}{4m^2} + \frac{4EIz_n^4}{mL^4}}, \tag{48}$$

and one can obtain, for small c and when the values of z_n from (47) are real or close to the real axis (this situation happens for $\hat{k}_{ts}$ large, positive or negative), approximate values of the zeros. The absolute value gives a good approximation for the location of antiresonances:

$$s_{zeros} \approx \pm i\frac{2|z_n|^2}{L^2}\sqrt{\frac{EI}{m}}. \tag{49}$$

In the special case $\hat{k}_{ts} = -8$, in addition to the zeros in (48), there is one additional pair of real zeros, one at the origin and the other at $s = -c/m$.

The limit cases can be treated analogously. If $\hat{k}_{ts} = 0$, then

$$n_{22}^0 = \frac{-4L^3}{3}\prod_{n=1}^{\infty}\left[1 - \frac{L^4\lambda^4}{c_n^4}\right], \tag{50}$$

where the c_n are the solutions of (42). One has then alternating zeros in the positive and negative real axis,

$$s_{zeros}^0 = -\frac{c}{2m} \pm \sqrt{\frac{c^2}{4m^2} + \frac{EIc_n^4}{mL^4}}. \tag{51}$$

Note that in this case, subsystem 22 is non-minimum phase.

If $\hat{k}_{ts} \to \infty$, then

$$n_{22}^\infty = -\frac{L^3}{6}\prod_{n=1}^{\infty}\left[1 + \frac{L^4\lambda^4}{c_n^4}\right]^2, \tag{52}$$

where the c_n are defined in (42). The zeros have then multiplicity two, and are given by the expression

$$s_{zeros}^\infty = -\frac{c}{2m} \pm \sqrt{\frac{c^2}{4m^2} - \frac{EIc_n^4}{mL^4}}. \tag{53}$$

The zeros appear in complex conjugate pairs, of multiplicity two, with negative real part, so the subsystem is minimum phase in this case.

In figure 8 we represent the location of the zeros of subsystem 22 when $\hat{k}_{ts}$ changes. The diagram shows the rather complex zero dynamics for different values of $\hat{k}_{ts}$.

The most interesting qualitative feature of figure 8 is how subsystem 22 changes from pairs of zeros in the real axis (alternating positive and negative) at $\hat{k}_{ts} = 0$ (circles in the diagram) to a situation in which there are pairs of complex conjugate zeros located in the LHP, for $\hat{k}_{ts} \to \pm\infty$ (crosses in the diagram). Numerically studying this behaviour for intermediate values of $\hat{k}_{ts}$, we found that for any finite value of $\hat{k}_{ts}$ there are an *infinite number* of RHP zeros, i.e. the subsystem 22 (base excitation to slope measurement) is non-minimum phase. For increasing $|\hat{k}_{ts}|$, an increasing number of low frequency zeros move into the LHP (the first cross being at $\hat{k}_{ts} = 8$), but still an infinity of (high frequency) zeros can be found in the RHP. Only in the limit case $\hat{k}_{ts} \to \pm\infty$ *all* zeros are in the LHP, i.e. the subsystem is minimum phase. Note that this behaviour is only possible with an infinite number of zeros and could not be accurately captured by any finite-dimensional approximation of the system. RHP zeros impose limitations in system performance and makes difficult the implementation of model-based control [20].
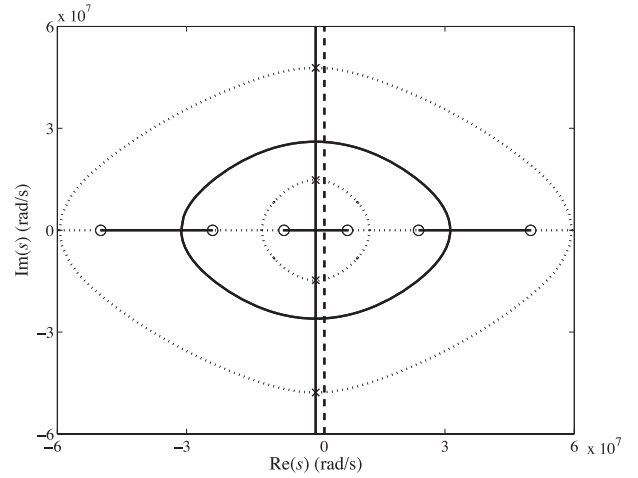
Figure 8. Location of zeros with $\hat{k}_{ts}$. Circles mark zeros at $\hat{k}_{ts} = 0$ and crosses at $\hat{k}_{ts} \to \infty$. Solid lines and dotted lines describe, respectively, the movement of zeros for positive and negative $\hat{k}_{ts}$. The dashed line is the imaginary axis.

8. Step response

The step response of the subsystem ij in the time domain $y_{ij}(t)$ is obtained applying the inverse Laplace transform to the product of the subsystems and unit step $(1/s)$ transfer functions [7]:

$$y_{ij}(t) = \frac{1}{2\pi i}\int_{c-i\infty}^{c+i\infty}e^{st}\frac{G(s)}{s}. \tag{54}$$

An exact solution to this integral is found by direct application of the residue theorem [31],

$$y_{ij}(t) = \sum_{k=0}^{\infty}\text{Res}\left[e^{st}\frac{G(s)}{s}\right]_{s=s_k}, \tag{55}$$

where s_k are the singular points, i.e. the poles, of $G(s)/s$.

Since (36) is an exact expression for all the poles of the transfer function $G(s)$, the problem is reduced to calculate the residues. As the contribution of high order poles rapidly diminishes, i.e. the series (29) converges very fast, only the first n poles contributing to the system response will be considered in the sum. This truncation can be considered a very accurate estimation of the sum. All the subsystems considered above have no poles at zero, except when $\hat{k}_{ts} = -1$ (which leads to an instable system and hence its step response is of no interest). Thus, the integrand in (54), where the residues are evaluated, have a single pole at $s = 0$, corresponding to the step response transfer function $1/s$. The infinite product expansion of the denominator obtained in section 6 gives the remaining poles. Therefore, the step response is given by

$$y_{ij}(t) = G(0) + \sum_{k=1}^{\infty}\frac{e^{s_kt}}{s_k}\text{Res}\left[G(s)\right]_{s=s_k}. \tag{56}$$

$G(0)$ is evaluated using the expressions for numerators and common denominator given in sections 6 and 7. The residues of the transfer function can be evaluated by application of the
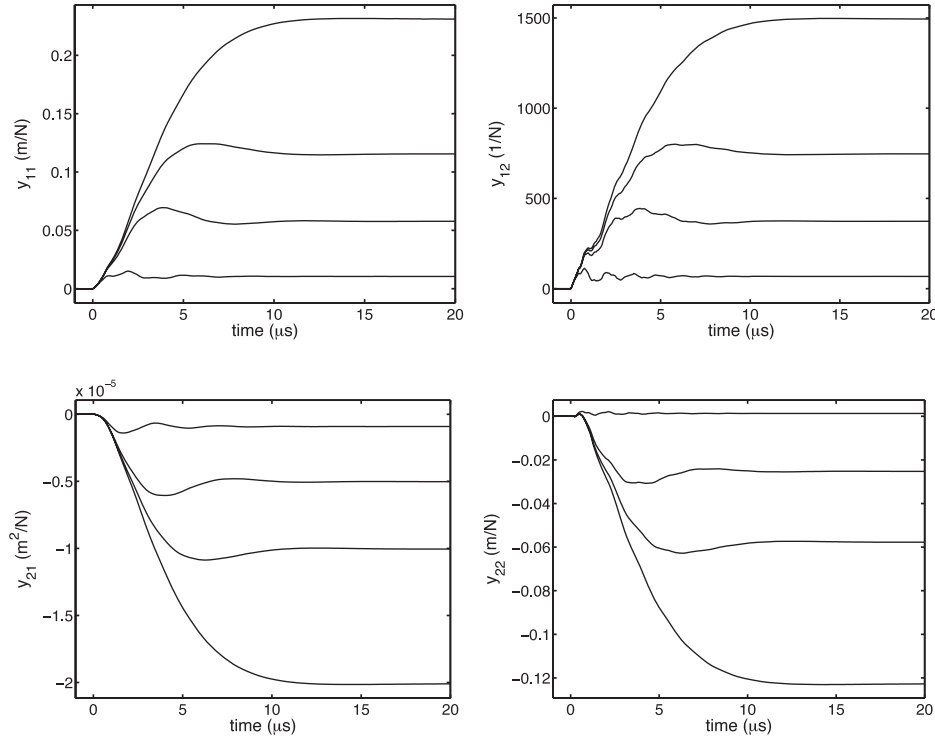
Figure 9. Response to a unit force step input of the different subsystems considered with varying contact stiffness ($\hat{k}_{ts} = -1, 0, 1$ and 10). The damping factor considered was of $c = 0.3$ kg ms^{-1}. The response amplitude decreases with increasing contact stiffness.

L'Hospital rule [32]

$$\mathrm{Res}\left[G(s)\right]_{s=s_k} = N(s_k) \lim_{s \to s_k} \frac{s - s_k}{D(s)} = \frac{N(s_k)}{D'(s_k)}, \qquad (57)$$

where $N(s_k)$ and $D(s_k)$ are the numerator and denominator of the transfer function evaluated at s_k, respectively, and $D'(s_k)$ denotes the derivative of the denominator with respect to s. Introducing (57) in (56) and applying the chain rule, the step response to a unit force is given as

$$y_{ij}(t) = G(0) + \sum_{k=1}^{n} \frac{\mathrm{e}^{s_k t}}{s_k} \frac{N(\lambda(s_k))}{D'(\lambda(s_k))\lambda'(s_k)}. \qquad (58)$$

Figure 9 shows the response to a unit force step of the different system configurations with varying contact stiffness $\hat{k}_{ts} = -1, 0, 1, 10$. The damping factor used was of $c = 0.3$ kg ms^{-1} (corresponding to a liquid environment) to better show the dynamics of the system. The response amplitude decreases with increasing contact stiffness and increases cantilever oscillations before the steady state is reached.

The non-minimum phase behaviour in a certain range of $\hat{k}_{ts}$ for the subsystem corresponding to g_{22} is observed in the transient response of the cantilever. To clearly illustrate this effect figure 10 shows the normalized force step response of g_{22} with varying contact stiffness close to zero, $\hat{k}_{ts} = -0.5, 0, 1, 3$ (normalization to a unit maximum response). The system reacts at the very beginning against the input, corresponding to its non-minimum phase character. The amplitude of the reaction at the beginning increases with increasing $\hat{k}_{ts}$. Note that, due to the normalization, the characteristic reaction appears more pronounced compared to the plots in figure 9.
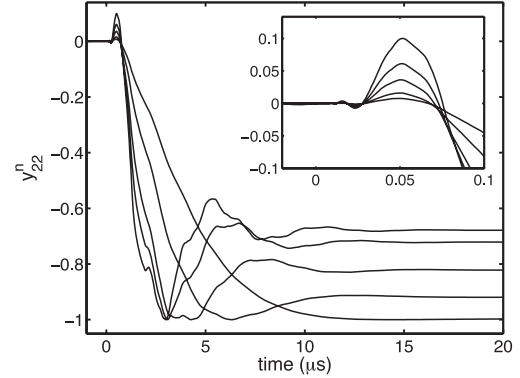
Figure 10. Response to a unit force step input of the normalized step response y_{22}^n with varying contact stiffness close to zero. The used contact stiffness are $\hat{k}_{ts} = -0.5, 0, 1, 2$ and 3. The normalized steady state response increments with increasing contact stiffness $\hat{k}_{ts}$. The damping factor considered was of $c = 0.3$ kg ms^{-1}. The insert shows a zoom of the response at the very beginning where the non-minimum phase character of the system produces an initial response of the system against the given force input.

This example illustrates that the properties of the system transfer function gives direct insight in cantilever transient response. Other models using simplified AFM dynamical models or considering a finite number of modes will not describe accurately the dynamics of the system, unless they include the zero dynamics, which plays an important role as seen in (58). It is also worth noting that the impulse response of the system can be easily found using the previous

derivation. The transfer function of the impulse is the unit function, without any pole at $s = 0$. Thus, it is only necessary to eliminate the term corresponding to the pole at $s = 0$ in (58). One direct application of the transient response of the considered system is the analysis of force spectroscopy curves obtained by the AFM [28].

9. Conclusions

In this work the dynamics of an AFM cantilever involved in force spectroscopy has been investigated using an exact system-theoretic approach based on the infinite dimensional transfer function of a rectangular AFM cantilever. The transfer functions obtained for different input/output configurations indicate different behaviours of the system, especially in the system zeros which greatly affects the frequency and transient response. From the transfer functions, the dynamics of the system were analysed using the Bode plot, poles and zeros locus plot, and transient response to a force step input. The frequency responses of the different system configurations verify that the dynamics are greatly affected by varying force gradients. Poles are common to all system configurations and are obtained using the infinite product expansions of the system. The analysis of the system poles allows us to detect an instable system behaviour for the range $\hat{k}_{ts} \in (-\infty, -1)$. The infinite product expansion of transfer function numerator for the different system configurations yields the system zeros. For the case where the cantilever is actuated by a distributed force and the cantilever slope is used as output the zeros are additionally affected by the contact stiffness. For this case the system is non-minimum in phase for any finite value of $\hat{k}_{ts}$ and only in the limit case (pinned cantilever) the system is minimum phase. The non-minimum phase behaviour is manifest in the phase shift of the Bode plot and in the initial transient response to a step force input.

Therefore, our study demonstrates that a detailed theoretical analysis is important because the transfer characteristics critically depends on the system configuration and must be considered in the quantitative analysis of AFM experiments, especially those related to force spectroscopy. The inputs and outputs of the AFM model have to be carefully selected to match experimental conditions.

The description of the dynamic behaviour has direct applications to the analysis of force spectroscopy experiments:

- the frequency shift and variations of the amplitude response due to varying contact stiffness can be used in dynamic experiments to quantify viscoelastic properties of tethered molecules;
- the force step response can be analysed to study the deformation and adhesion properties of the tethered molecules in single-molecule AFM force spectroscopy in detail;
- considering fluctuations of the specimen itself, for example by fluctuations in the molecular structure, the cantilever acts as a mechanical filter which exhibits band pass characteristics even at high frequencies (close to higher eigenmode resonances) and a band stop character at frequencies close to the transmission minima.

Additionally, only extended beam models can capture important features such as pole-zero cancellations or non-minimum phase response. The possibility of non-minimum phase response in AFM is highly important for the design of inverse filters as they are required, for example, in the inversion of the signal path or for certain control applications. The presence of zeros in the right half plane of the dynamic system immediately implies that the inverse system is instable. Thus, for control application and advanced signal processing the location of the zeros in the Laplace plane has to be evaluated very carefully considering the actual loading conditions as well as actuation and detection.

In conclusion, the example of an idealized rectangular beam revealed general properties of the cantilever dynamics in AFM. In order to analyse experimental configurations of course further aspects such as the finite spot size of the detection laser or the actual geometry of the cantilever have to be considered. Here, a similar analysis based on an accurate finite element model might be necessary. Additionally, an experimental identification of the system's poles and zeros [33] might be required. To this end the properties of an idealized beam as discussed here can serve as a starting point for a customized analysis. Moreover, a precise knowledge of the transfer characteristics of the force sensor expands the possibilities for model-based control and observer design to improve state-of-the-art performance in spectroscopy, microscopy and nanomanipulation.

Acknowledgments

References

[1] Rief M, Oesterhelt F, Heymann B and Gaub H E 1997 *Science* **275** 1295–7
[2] Oberhauser A F, Hansma P K, Carrion-Vazquez M and Fernandez J M 2001 *Proc. Natl Acad. Sci. USA* **98** 468–72
[3] Fernandez J M and Li H 2004 *Science* **303** 1674–8
[4] Gelbert M, Roters A, Schimmel M and Johannsmann D 1999 *Surf. Interface Anal.* **27** 572–7
[5] Bippes C A, Humphris A D L, Stark M, Müller D J and Janovjak H 2006 *Europhys. Biophys. J.* **35** 287–92
[6] Humphris A D L, Tamayo J and Miles M J 2000 *Langmuir* **16** 7891–4
[7] Franklin G F, Powell J D and Emami-Naeini A 1986 *Feedback Control of Dynamic Systems* (Reading, MA: Addison-Wesley)
[8] Stark M, Stark R W, Heckl W M and Guckenberger R 2002 *Proc. Natl Acad. Sci. USA* **99** 8473–8
[9] Gotsmann B, Seidel C, Anczykowski B and Fuchs H 1999 *Phys. Rev.* B **60** 11051–61
[10] Chang W J, Fang T H and Weng C I 2004 *Nanotechnology* **15** 427–30
[11] Sahoo D R, Sebastian A and Salapaka M 2003 *Appl. Phys. Lett.* **83** 5521–3
[12] Yen J, Lin I and Lee C 2005 *Rev. Sci. Instrum.* **76** 036103
[13] Burnham N A, Gremaud G, Kulik A J, Gallo P J and Oulevey F 1996 *J. Vac. Sci. Technol.* B **14** 1308–12
[14] García R and Pérez R 2002 *Surf. Sci. Rep.* **47** 197–301

[15] Rabe U, Turner J and Arnold W 1998 *Appl. Phys.* A **66** S277–82

[16] Stark R W, Schitter G, Stark M, Guckenberger R and Stemmer A 2004 *Phys. Rev.* B **69** 085412

[17] Rabe U, Janser K and Arnold W 1996 *Rev. Sci. Instrum.* **67** 3281–93

[18] Hirsekorn S 1998 *Appl. Phys.* A **66** 249–54

[19] Dareing D W, Thundat T, Sangmin J and Nicholson M 2005 *J. Appl. Phys.* **97** 084902

[20] Spector V A and Flashner H 1990 *ASME J. Dyn. Syst. Meas. Control* **112** 186–93

[21] Goodson R E 1970 *Simulation* **15** 255–63

[22] Rubio-Sierra F J, Vázquez R and Stark R W 2006 *IEEE Trans. Nanotechnol.* **5** 692–700

[23] Florin E L, Moy V T and Gaub H E 1994 *Science* **264** 415–7

[24] Putman C A J, der Werf K O V, Grooth B G D, Hulst N F V and Greva J 1994 *Appl. Phys. Lett.* **64** 2454–6

[25] Drobek T, Stark R W and Heckl W M 2001 *Phys. Rev.* B **64** 045401

[26] Rugar D, Mamin H J, Erlandsson R, Stern J E and Terris B 1988 *Rev. Sci. Instrum.* **59** 2337–40

[27] Meyer G and Amer N M 1990 *Appl. Phys. Lett.* **56** 2100–1

[28] Cappella B and Dietler G 1999 *Surf. Sci. Rep.* **34** 1–104

[29] Rabe U, Janser K and Arnold W 1996 *Rev. Sci. Instrum.* **67** 3281–93

[30] Hao H O, Baró A M and Sanz J J 1991 *J. Vac. Sci. Technol.* B 249–54

[31] Bronstein I N, Semendjajew K A, Musiol G, Musiol H and Mühlig H 1977 *Taschenbuch der Mathematik* (Frankfurt am Main: Harri Deutsch)

[32] Apostol T M 1967 *Calculus* vol 1 (New York: Wiley)

[33] Stark M, Guckenberger R, Stemmer A and Stark R W 2005 *J. Appl. Phys.* **98** 114904